BJR



Received: 5 December 2015 | Revised: 8 February 2016 | Accepted: 25 February 2016

http://dx.doi.org/10.1259/bjr.20151028

Cite this article as:
Norman W, Jawad N, Jones R, Taylor AM, Arthurs OJ. Perinatal and paediatric post-mortem magnetic resonance imaging (PMMR): sequences and technique. *Br J Radiol* 2016; **89**: 20151028.

## REVIEW ARTICLE

# Perinatal and paediatric post-mortem magnetic resonance imaging (PMMR): sequences and technique

**[1,2]WENDY NORMAN, DCR(R), DRI, [3]NOORULHUDA JAWAD, MBBS, FRCR, [1,2]ROD JONES, DCR(R), MSc, [1,2]ANDREW M TAYLOR, FRCR, MD, and [3,4]OWEN J ARTHURS, FRCR, PhD**

[1]Cardiorespiratory Division, Great Ormond Street Hospital for Children NHS Foundation Trust, London, UK
[2]Centre for Cardiovascular Imaging, UCL Institute of Cardiovascular Science, London, UK
[3]Department of Radiology, Great Ormond Street Hospital for Children NHS Foundation Trust, London, UK
[4]Institute of Child Health, UCL, London, UK

Address correspondence to: Dr Owen J Arthurs
E-mail: *owen.arthurs@gosh.nhs.uk*

## ABSTRACT

As post-mortem MRI (PMMR) becomes more widely used for investigation following perinatal and paediatric deaths, the best possible images should be acquired. In this article, we review the most widely used published PMMR sequences, together with outlining our acquisition protocol and sequence parameters for foetal, perinatal and paediatric PMMR. We give examples of both normal and abnormal appearances, so that the reader can understand the logic behind each acquisition step before interpretation, as a useful day-to-day reference guide to performing PMMR.

## INTRODUCTION

Post-mortem (PM) imaging is becoming increasingly used in both adult and paediatric practice. In adults, multiphase post-mortem whole-body CT angiography is now widely used as the first-line investigation,[1,2] but post-mortem MRI (PMMR) is becoming the accepted modality of choice following foetal and perinatal deaths.[3,4] The correct acquisition, interpretation and reporting of such images becomes increasingly important as more practitioners begin to develop and provide these services. Although the diagnostic accuracy of perinatal PMMR in general has been shown to be high following specialist interpretation,[5] PMMR is prone to errors, made by mis-interpretation of normal PM changes and PM artefacts as pathology, and *vice versa*.[6,7] Optimal image acquisition is the first step towards minimizing interpretation errors.

Optimization of post-mortem imaging requires different considerations to that of live imaging. Surface coils should be placed according to optimal signal rather than patient comfort, although the body may contour to the coil if left in place for over an hour. Electrocardiogram triggering and respiratory gating is not required, although very small specimens (<100-g body weight) may need to be stabilized securely to avoid the physical vibration which can occur with particular pulse sequences, dependent upon acoustic frequencies. As the duration of a single sequence does not need to be shortened to meet the physical comfort needs of the patient and distorted anatomy may make conventional imaging planes difficult to identify, we advocate three-dimensional (3D) isotropic sequences (equal voxels in all dimensions) wherever possible, to both reduce overall imaging time and produce the best possible image quality.

However, not all groups who have published within the perinatal PMMR literature use 3D sequences. A comprehensive literature search revealed over 15 different protocols described at 1.5 T or 3.0 T since perinatal PMMR began almost 20 years ago. A summary of the main published protocols is given in Table 1,[8–20] together with a summary of our group's current protocol which is described in this article in more detail. We excluded studies which described only the adult population, higher field strengths (7.0 or 9.4 T) MR, and reference the first article where more than one article from the same group has used the same protocol.

We noticed that almost all authors use some form of two-dimensional (2D) $T_2$ weighted (T2-w) sequences to assess the brain. Some groups also describe using $T_1$ weighted (T1-w) sequences[11,13,19] or 3D T1-w sequences,[10,17,18] but most authors report that T1-w brain imaging added little, generally due to a lack of tissue contrast.[9,14] Only within the past 5 years have some authors begun to use susceptibility-weighted sequences to detect subtle haemorrhage.[16,17] Most groups do not perform separate spinal imaging but include it as part of body imaging. Since 2010, there has

Table 1. Comparison of published sequence parameters for post-mortem foetal MRI

| Sequence | Brookes et al,[8] 1996 | Woodward et al,[9] 1997 | Brookes et al,[10] 1999 | Huisman et al,[11] 2002 | Griffiths et al,[12] 2003 | Alderliesten et al,[13] 2003 | Breeze et al,[14] 2006 | Sarikouch et al,[15] 2008 | Sieswerda-Hoogendoorn and van Rijn,[16] 2010 | Thayyil et al,[17] 2011 | Prodhomme et al,[18] 2012 | Cannie et al,[19] 2012 | Sandaite et al,[20] 2013 | Our current protocol |
|---|---|---|---|---|---|---|---|---|---|---|---|---|---|---|
| Brain imaging | | | | | | | | | | | | | | |
| 3D T1-w | – | – | Sag MP-RAGE | 2D SE. Ax/ Cor/Sag | – | 2D Sag/Ax | – | – | Sag and Cor/ Ax recons | 3D FLASH | VIBE | Axial TurboFLASH | – | 3D FLASH |
| 2D T2-w | SE Cor/Sag | FSE Ax | SE. Cor/Sag | SE. Ax/ Cor/Sag | FSE Ax/ Cor/Sag | TSE Ax | FSE-XL Ax/ Cor/Sag | – | Ax | 2D DESTIR | – | HASTE Ax/ Cor/Sag | – | DESTIR Ax/Cor |
| 2D $T_1$ SWI | – | – | – | – | – | – | – | – | FLASH | GE | – | – | – | Axial |
| DWI | – | – | – | – | – | – | – | – | – | (*b*-value 0, 500, 1000) | – | – | – | (*b*-value 0, 500, 1000) |
| Other | | 3D T2-w FSE Cor | | | | | | | | 3D CISS | 3D T2-w TRUFISP | | | |
| Spine imaging | | | | | | | | | | | | | | |
| 3D T1-w | – | – | – | – | – | – | – | – | – | 3D FLASH | – | – | – | 3D FLASH |
| 3D T2-w | – | – | – | – | FSE Ax/ Cor/Sag | – | – | – | – | 3D CISS | – | – | – | 3D CISS |
| Body imaging | | | | | | | | | | | | | | |
| 3D T1-w | – | – | Sag MP-RAGE | 2D SE. Ax/ Cor/Sag | – | 2D Cor/Sag | – | – | Cor | VIBE | VIBE | Ax TurboFLASH | – | VIBE |
| 3D T2-w low res | – | – | – | – | – | – | – | – | Cor and Ax/ Sag recons | TSE | TRUFISP | HASTE Ax/ Cor/Sag | – | TSE |
| 3D T2-w high res | – | FSE Cor | – | – | – | – | – | – | – | CISS | – | – | Yes: HASTE | CISS |
| 2D T2-w | SE. Cor/Sag | FSE Ax | SE. Cor/Sag | FSE Ax/ Cor/Sag | FSE Ax/ Cor/Sag | TSE Cor/Sag | FSE-XL Ax/ Cor/Sag | Yes: TSE | – | – | – | – | – | Low res. Ax |
| DWI | – | – | – | – | – | – | – | – | – | – | – | – | – | (*b*-value 0, 500, 1000) |

2D, two-dimensional; 3D, three-dimensional; Ax/Cor/Sag, axial, coronal or sagittal acquisition, respectively; CISS, constructive interference steady state; DESTIR, dual-echo short-tau inversion recovery; DWI, diffusion-weighted imaging; FLASH, fast low angle shot; FSE, fast spin echo; FSE-XL, fast spin echo-acclerated; GE, gradient echo; HASTE, half-Fourier acquisition single-shot turbo spin-echo; low res., low resolution; MP-RAGE, magnetization prepared rapid acquisition; SE, spin echo; SWI, susceptibility-weighted imaging; T1-w, $T_1$ weighted; T2-w, $T_2$ weighted; TRUFISP, true fast imaging with steady-state precession; TSE, turbo spin echo; TurboFLASH, fast imaging using extremely low angle shot; VIBE, volumetric interpolated breath-hold examination.

Table 2. Sequence parameters for post-mortem MRI (PMMR) in a neonate or infant

| Sequence | FOV (mm) | Slice thickness (mm) | Matrix | Voxel size (mm) | TR (ms) | TE (ms) | Flip angle (°) | Averages (NEX/ NSA) | Number slices and gap | Approximate length of sequence (min) |
|---|---|---|---|---|---|---|---|---|---|---|
| Brain imaging | | | | | | | | | | |
| 3D FLASH T1-w (sag) | 256 | 1 | 256/256 | 1.0 × 1.0 × 1.0 | 11 | 4.9 | 15 | 3 | 60 per slab | 5.44 |
| 2D DESTIR T2-w (axial and coronal) | 100 | 2 | 172/256 | 0.4 × 0.4 × 2.0 | 5460 | 16 and 115 | 150 | 6 | 18 (1 mm) | 13.46 |
| 2D GRE $T_1$ HEME (axial) | 100 | 4 | 120/256 | 0.5 × 0.4 × 4.0 | 800 | 26 | 20 | 4 | 18 (0 mm) | 6.26 |
| DWI (axial) (*b*-values 0,500,1000) | 230 | 5 | 128/128 | 1.8 × 1.8 × 5.0 | 2700 | 96 | 90 | 3 | 19 (0 mm) | 1.06 |
| Spine imaging | | | | | | | | | | |
| 3D CISS T2-w (sag) | 150 | 1.5 | 128/256 | 0.6 × 0.6 × 1.5 | 9.1 | 4.5 | 70 | 8 | 12 per slab | 4.24 |
| 3D FLASH T1-w (sag) | 150 | 1.25 | 128/256 | 0.6 × 0.6 × 1.3 | 11 | 5.3 | 15 | 10 | 16 per slab | 3.19 |
| Body imaging | | | | | | | | | | |
| 3D T2-w TSE (cor) | 200 | 0.8 | 160/256 | 0.8 × 0.8 × 0.8 | 3500 | 275 | Variable | 2 | 72 per slab | 6.20 |
| 3D T1-w VIBE (cor) | 200 | 0.8 | 160/256 | 0.8 × 0.8 × 0.8 | 5.9 | 2.4 | 25 | 8 | 72 per slab | 5.52 |
| 3D CISS T2-w (axial) (cardiac) | 150 | 0.6 | 192/256 | 0.6 × 0.6 × 0.6 | 5.6 | 2.5 | 54 | 10 | Adjust to cover heart and entire lung fields | 29.26 |
| 2D T2-w tirm (axial) ($T_i$ = 150) | 180 | 5 | 160/256 | 0.7 × 0.7 × 5.0 | 5080 | 109 | 150 | 5 | Adjust to cover body and upper legs | 6.58 |
| DWI | As for the head with a greater number of slices to cover the chest, abdomen and pelvis | | | | | | | | | 1.06 |

2D, two-dimensional; 3D, three-dimensional; Cor/Sag, coronal or sagittal acquisition, respectively; CISS, constructive interference steady state; DESTIR, dual-echo short-tau inversion recovery; DWI, diffusion-weighted imaging; FLASH, fast low angle shot; FOV, field of view; GRE, gradient recalled echo; HEME, $T_2$ weighted gradient recalled echo sequence; NEX, number of excitations; NSA, number of signal averages; T1-w, T1 weighted; T2-w, T2 weighted; TE, echo time; Ti, inversion time; TIRM, turbo inversion magnitude sequence; TR, repetition time-; TSE, turbo spin echo; VIBE, volumetric interpolated breath-hold examination.

Table 3. Sequence parameters for post-mortem MRI in a child less than 2 years of age

| Sequence | FOV (mm) | Slice thickness (mm) | Matrix | Voxel size (mm) | TR (ms) | TE (ms) | Flip angle (°) | Averages (NEX/ NSA) | Number slices and gap | Approximate length of sequence (min) |
|---|---|---|---|---|---|---|---|---|---|---|
| Brain imaging | | | | | | | | | | |
| 3D FLASH T1-w (sag) | 256 | 1 | 224/256 | 1.0 × 1.0 × 1.0 | 11 | 4.9 | 15 | 1 | 160 per slab | 4.20 |
| 2D DESTIR T2-w (axial and coronal) | 200 | 4 | 216/320 | 0.7 × 0.6 × 4.0 | 6180 | 14 and 115 | 150 | 1 | 22 (1 mm) | 3.19 |
| 2D GRE $T_1$ HEME (axial) | 200 | 5 | 144/256 | 1.0 × 0.8 × 5.0 | 800 | 26 | 20 | 2 | 18 (0 mm) | 3.52 |
| DWI (*b*-values 0, 500, 1000) | 230 | 5 | 128/128 | 1.8 × 1.8 × 5.0 | 2700 | 96 | 90 | 3 | 19 (0 mm) | 1.06 |
| Spine imaging | | | | | | | | | | |
| 2D T2-w TSE (sag) | 300 | 3 | 272/320 | 1.1 × 0.9 × 3.0 | 3050 | 109 | 170 | 3 | 11 per slab | 5.43 |
| 3D FLASH T1-w (sag) | 350 | 1.4 | 144/256 | 1.4 × 1.4 × 1.4 | 11 | 4.9 | 15 | 6 | 32 per slab | 5.06 |
| Body imaging | | | | | | | | | | |
| 3D T2-w TSE (cor) | 360 | 1.4 | 226/256 | 1.4 × 1.4 × 1.4 | 3500 | 173 | Variable | 1 | 96 per slab | 3.42 |
| 3D T1-w VIBE (cor) | 360 | 1.4 | 224/256 | 1.4 × 1.4 × 1.4 | 5.9 | 2.4 | 25 | 5 | 72 per slab | 6.33 |
| 3D CISS T2-w (axial) (cardiac) | 150 | 0.6 | 192/256 | 0.6 × 0.6 × 0.6 | 5.6 | 2.5 | 54 | 10 | Adjust to cover heart and entire lung fields | 29.26 |
| 2D T2-w tirm (axial) ($T_i = 150$) | 300 | 5 | 168/256 | 1.2 × 1.2 × 5.0 | 8390 | 108 | 150 | 4 | Adjust to cover body and upper legs | 4.47 |
| DWI | As for the head with a greater number of slices to cover the chest, abdomen and pelvis | | | | | | | | | 1.06 |

2D, two-dimensional; 3D, three-dimensional; CISS, constructive interference steady state; cor, coronal; DESTIR, dual-echo short-tau inversion recovery; DWI, diffusion-weighted imaging; FLASH, fast low angle shot; FOV, field of view; GRE, gradient recalled echo; HEME, $T_2$ weighted gradient recalled echo sequence; NEX, number of average; NSA, number of signal averages; sag, sagittal; T1-w, $T_1$ weighted; T2-w, $T_2$ weighted; TE, echo time; Ti, inversion time; TIRM, turbo inversion recovery magnitude sequence; TR, repetition time; TSE, turbo spin echo; VIBE, volumetric interpolated breath-hold examination.

Figure 1. Normal post-mortem MRI (PMMR), brain imaging. Routine PMMR of the brain in a normal 3-month-old infant, whose cause of death was undetermined (sudden unexpected death in infancy). (a) Conventional $T_1$ weighted (T1-w); (b, c) short and long dual-echo short-tau inversion recovery (echo time, 15 and 115 ms, respectively); (d) susceptibility-weighted imaging (SWI); and (e) diffusion-weighted images are shown to demonstrate the typical signal to noise ratio and contrast to noise ratio using the parameters listed in Table 3. (d) SWI highlights normal venous congestion.

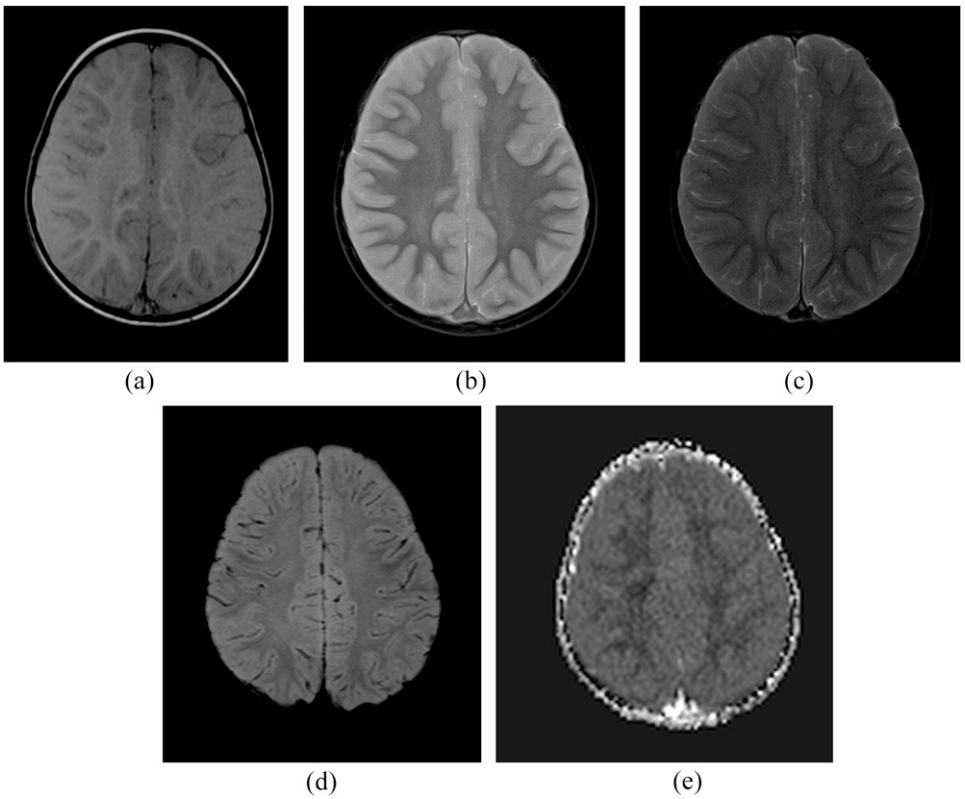


been a move from 2D to 3D body acquisitions, mainly using T2-w sequences.[16] To our knowledge, we are the only group to routinely use diffusion-weighted sequences as part of our standard PMMR protocol for the brain or body.

In this article, we outline our departmental protocol for foetal, perinatal and paediatric PMMR. We include a description of the types of sequences used for brain and body imaging, with detailed sequence parameters (Tables 2 and 3), as well as discussing additional sequences such as diffusion-weighted, and susceptibility-weighted imaging (SWI). We outline the advantages of each sequence, what particular normal or abnormal findings can be usefully demonstrated and age-related adaptations. As macrostructural and microstructural changes vary according to different gestational ages, several sequence parameters may need to be further adjusted to account for the different chemical composition of the brain, spine and body organs. Normal physiological changes at PMMR have been described in more detail elsewhere.[6]

Clearly, image quality is multifactorial, dependent upon field strength, specimen size and coil selection. The most readily optimized of these is probably coil selection: phased-array coils with multiple elements lying in close proximity to the region of interest would be an ideal solution. Specific manufacturers have provided different solutions: in general, a dedicated head coil for neuroimaging, spine (including a neck matrix coil) and phase array matrix body coil for body imaging will suffice. Occasionally in larger children, a two-stage acquisition may necessitate movement of the phase array coil lower down the body to include the pelvis and legs. For smaller foetuses, the head coil may provide both adequate head and body coverage, and usually, the high matrix of head coils provides good signal to noise ratio. Smaller foetuses may also require padding to stabilize the body from sequence-induced movement through vibration.

The sequences and protocols outlined here are defined for a 1.5-T Siemens Avanto™ machine (Siemens Medical Solutions, Erlangen, Germany), with conventional head and body coils, but can be easily adapted and interpreted for other machine manufacturers. We provide the starting parameters which should provide appropriate imaging for those new to the specialty, upon which further modifications could be made dependent upon the specific machine and gestation of the case.

## BRAIN IMAGING

### $T_1$ weighted imaging of the brain

A high-resolution isotropic 3D data set is first acquired. We use a 3D multislice gradient-echo fast low angle shot (FLASH)

Figure 2. Intraventricular haemorrhage on post-mortem MRI (PMMR). Routine PMMR of the brain in stillbirth at 28 weeks of gestation. (a) Conventional $T_1$ weighted, (b) short echo time short-tau inversion recovery and (c) susceptibility-weighted imaging show typical intraventricular haemorrhage. Small amounts of intraventricular haemorrhage can be a normal finding in premature infants at autopsy.

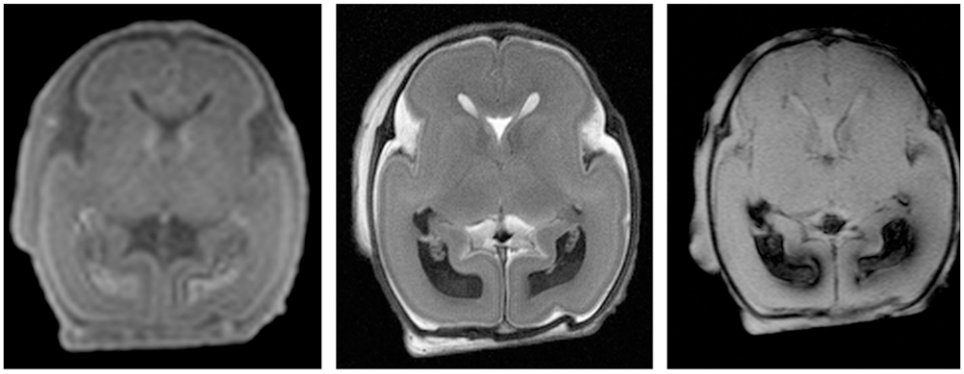


which combines a low flip angle radiofrequency (RF) pulse with rapid repetition to create a 3D data set in under 10 min. This allows excellent 3D visualization of the brain structures, and isotropic acquisition allows reformatting in any plane (Figure 1). This sequence should allow for assessment of cerebral anatomy, maturation of brain parenchyma and localization of vessels. T1-w imaging in general allows evaluation for high T1-w signal haemorrhage and calcification (Figure 1). The main disadvantage of T1-w post-mortem imaging is relatively low signal combined with low contrast.[9,14]

Foetal brain development follows a recognized pattern which is well documented elsewhere.[21–24] For example, the Sylvian fissure begins to appear at 16 weeks, parieto-occipital at 22 weeks, central sulcus at 26 weeks, and is almost complete by 34 weeks. Familiarity with normal brain development can help mis-interpretation: it is on this background that abnormal sulcation, including lissencephaly, polymicrogyria and schizencephaly, can be assessed. As well as cortical changes, progressive myelination from caudal to cephalad and dorsal to ventral across the brain, which continues into the first few years of infancy, can also affect the signal observed on PMMR images.

An alternative to a single 3D data set would be three separate acquisitions in the axial, coronal and sagittal planes, but the trade-off between the acquisition time of separate sequences, and the ability to reformat complex structures, is usually in favour of 3D imaging, particularly where there is no expected motion artefact from longer scan times. In addition, 3D imaging is inherently more efficient in terms of the signal-to-noise ratio per unit time (because all of the sample is excited with every RF pulse). Equivalent sequences on other manufacturer machines would be multiplanar spoiled gradient acquisition in the steady state (MPSPGR), T1-fast field echo (T1-FFE) or

Figure 3. Post-mortem MRI (PMMR) in antenatally diagnosed intracranial mass. Axial and coronal short-tau inversion recovery PMMR at 27 weeks of gestation depicts a complex heterogeneous intracranial teratoma with extension into the neck (a, b). Reproduced from Papadopoulou et al[25] with permission from John Wiley and Sons.

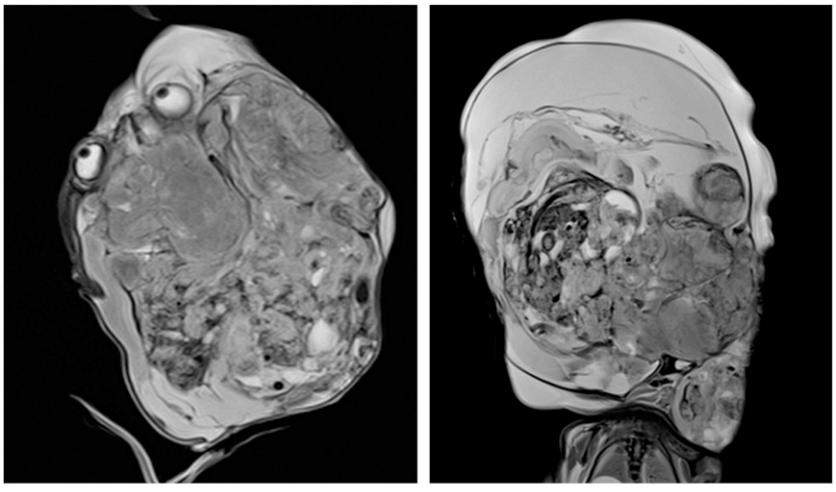

RF-spoiled fast field echo (FFE) sequences (GE, Fairfield, CT; Phillips, Amsterdam, Netherlands; Toshiba, Minato, Japan; respectively).

### $T_2$ weighted imaging of the brain

We subsequently acquire dual-echo short-tau inversion recovery (STIR) sequences in both axial and coronal planes (Figures 1–3). The STIR is a fat-suppression technique using short inversion times to acquire when $T_1$ (spin-lattice relaxation time) of fat is effectively zero. In this way, inversion recovery pulses emphasize the differences between $T_1$ properties of the brain and thus is very sensitive to the body fluid (long $T_1$ and long $T_2$). STIR sequences usually give higher contrast than conventional T1-w sequences allow.

Short echo time STIR gives a more proton density-weighted image, and longer echo time STIR more T2-w images (Figure 1), but the signal on both echoes decreases with reduction in $T_1$, $T_2$ or proton density, so that decreasing white matter signal may represent a normal increase in brain maturation. Foetuses and children under 2 years of age have increased water content in the brain compared with that of adults. The long echo STIR gives better $T_2$ contrast, allowing discrimination between grey and white matter, therefore greater detection of any lesions or detailed evaluation of complex abnormalities (Figure 3).[25] Other inversion recovery sequences (*e.g.* fluid attenuation inversion recovery or spectral attenuated inversion recovery) have been used in adult PM imaging but none optimized for paediatrics as yet. STIR or fast STIR sequences are widely used across manufacturers.

### Susceptibility-weighted imaging

Further brain sequences are useful for specific abnormalities. For example, a gradient-echo sequence that is sensitive to changes in the homogeneity of the local magnetic field, known as SWI, can be useful as the local signal is distorted by the ferromagnetic properties of haemoglobin breakdown.

SWI uses a fully flow-compensated long echo RF spoiled gradient-recalled echo pulse sequence. Both the magnitude images and filtered phase images are combined to provide an enhanced contrast magnitude image, referred to as susceptibility weighted. This makes it particularly useful for detecting venous blood, haemorrhage and iron storage, such as following trauma and vascular malformations such as cavernomas. Post-mortem venous congestion does not typically give a strong signal on SWI images, and thus its sensitivity to haemorrhage is particularly useful in PM cases (Figures 1 and 2). SWI sequences are broadly similar across manufacturers but are of typically poor resolution and so are cross-referenced to higher detail anatomical images.

### Diffusion-weighted imaging

Diffusion-weighted imaging (DWI) is a structural MRI technique which measures the diffusivity, or freedom of movement of water molecules, with the magnitude of signal loss between dephasing and rephasing gradients proportional to the diffusivity of the tissue.[26] It can be measured quantitatively and expressed as an apparent diffusion coefficient (ADC) value, such that a lower ADC value represents a tissue with more restricted water diffusivity. Several factors interact to change the ADC values, including water content, tissue cellularity and integrity of intracellular membranes.[27] DWI is performed using single shot spin-echo planar imaging in the axial plane, with diffusion gradients ($b$-values) of between 500 and 1000 s mm$^{-2}$ (Figure 1). Owing to the variation in water content and fat content in the immature unmyelinated brain, there is significant variation in normal ADC signal dependent upon foetal gestation and infant age. Reference to normal foetal values in the first instance is advised.[28] Appreciation of normal changes of the ADC with age will help avoid reporting errors of white matter abnormalities, particularly in early gestation foetuses. DWI sequences are broadly similar across manufacturers, but like SWI images are of typically poor resolution and so need to be cross-referenced to higher detail anatomical images.

Figure 4. Spinal post-mortem MRI. Sagittal low-resolution spinal $T_2$ weighted imaging of the spine at 30 weeks of gestation shows a neural tube defect (asterisk), allowing air to enter the spinal canal superiorly (arrow). Reproduced from Jawad et al[33] with permission from Elsevier.

Figure 5. Spinal post-mortem MRI. Spine imaging at 21 weeks of gestation. Sagittal reconstruction of a three-dimensional constructive interference steady state sequence (b) may give better signal and resolution than dedicated sagittal $T_2$ weighted imaging (a), particularly in smaller foetuses.

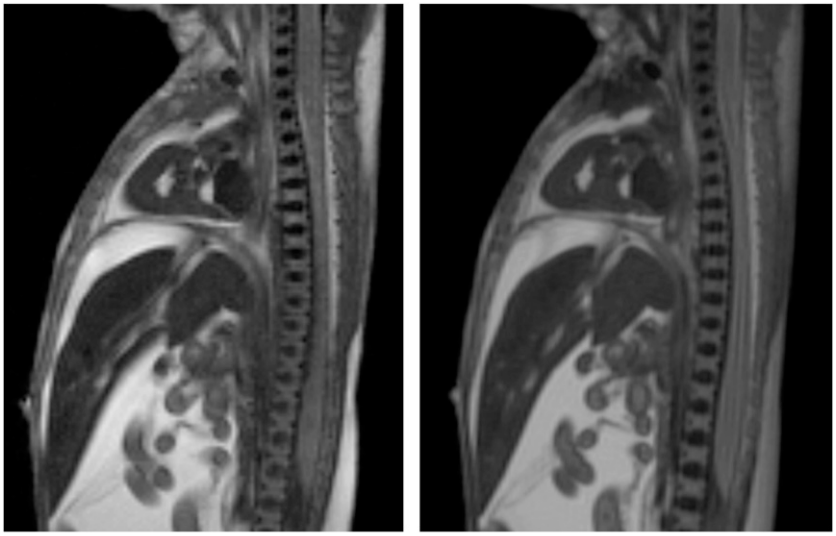

(a) (b)

DWI is likely to become more important in post-mortem brain imaging than previously thought, as water movement in the brain following death may reflect normal post-mortem changes. In the first few initial hours following death, tissue ischaemia will occur, followed by a period of cell lysis and membrane breakdown, then over a few days fluid redistribution occurs and slowly gas formation and putrefaction occur with decomposition.[29] ADC values typically increase following cell breakdown and autolysis, and several animal studies have suggested an effect of post-mortem interval on DWI changes in the brain.[30,31] This means that brain ADC may provide an indirect measure of water movement following death, such that it may be useful in forensic cases when the time of death is unknown.

Figure 6. Body post-mortem MRI. Coronal $T_2$ weighted (T2-w) (a) and $T_1$ weighted (T1-w) (b) images from a 33-week foetus with autosomal recessive polycystic kidney disease and pulmonary hypoplasia. T2-w images demonstrated the enlarged kidneys and hypoplastic lungs (a), and T1-w images show the normal high T1-w signal thyroid, meconium in the colon and high T1-w signal liver (b).

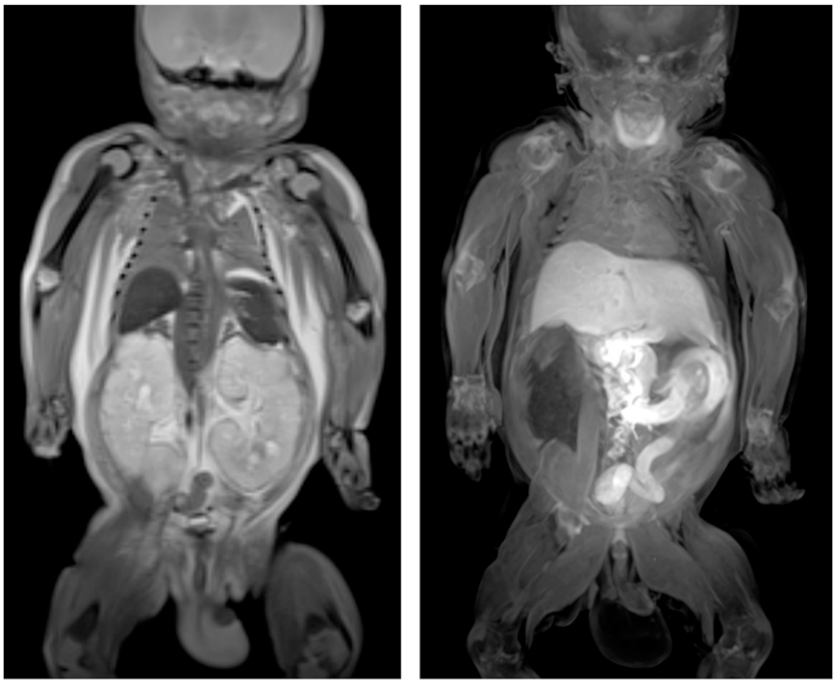

(a) (b)

## SPINE IMAGING

We perform dedicated T1-w and T2-w spinal imaging in neonates and children, similar to that which would be performed in life. We typically perform a conventional 2D spin echo sagittal T2-w sequence, and a narrow-field sagittal 3D $T_1$ FLASH sequence. Equivalent sequences on other manufacturer machines would be MPSPGR, T1-FFE or RF-spoiled FFE sequences (GE, Phillips, Toshiba, respectively). These sequences allow for accurate assessment of anatomy, and abnormalities of the spinal cord, discs, marrow signal and conus (Figure 4).[32,33] The smaller the foetus, the less important it is likely to be to acquire dedicated spinal imaging: often, sufficient detail is provided in the 3D volumetric acquisition of the body [3D constructive interference steady state (CISS), see the Body imaging section; Figure 5], which can be reconstructed into an oblique sagittal orientation. Although the volumetric acquisition takes longer, signal to noise ratio is typically higher than contiguous slice acquisition (Figure 5).

## BODY IMAGING

To image the body, which may include the spine, we mainly use high-resolution T2-w 3D sequences. These allow good tissue contrast and therefore characterization of organs as well as detection of abnormalities. All 3D data sets are acquired in the coronal plane, for better overall coverage, with isotropic resolution allowing for multiplanar reconstruction in other planes.

### $T_1$ weighted body imaging

High-resolution body contrast-to-noise can be obtained by a 3D volumetric interpolated breath hold examination sequence. This is a T1-w 3D FLASH ultrafast gradient echo with a fat-selective pre-pulse. Usually used as a breath-held contrast-enhanced sequence in live patients, at post-mortem, it can be used as a stand-alone acquisition. As an isotropic 3D acquisition with high contrast and T1-w, it gives excellent spatial resolution, with body imaging of foetuses down to 0.8 $mm^3$, around 1.2–1.4 $mm^3$ for the perinatal and paediatric population (Table 1). Although resolution is good, the signal to noise ratio is relatively low but can be increased with increasing averages as time allows. Equivalent ultrafast GE volumetric interpolated breath-hold examination sequences on other manufacturer machines would be fast SPGR or FAME/LAVA, THRIVE or fast FE sequences (GE, Phillips, Toshiba, respectively).

The foetal liver shows as high signal on T1-w and as low signal on T2-w images, secondary to increased iron content from foetal haemoglobin, together with protein and other metal ions (Figure 6). The gall bladder can be demonstrated from 20 weeks of gestation onwards. T1-w imaging is particularly useful at visualizing the pancreas, which can be difficult on T2-w imaging. The normal foetal large bowel usually contains meconium which has a high T1-w signal content (Figure 6). Other tissues with high T1-w signal include the thyroid and long bone physes.

### T2-w body imaging

We performed two T2-w imaging sequences of the body: typically a lower resolution coronal (overview) of the entire body from neck down to upper thigh, and then high-resolution isotropic acquisition of the thorax centred on the heart. The initial T2-w turbo spin-echo 3D volume gives a quick overview of body proportions, with isotropic resolution allowing multiplanar construction of all of the thoracoabdominal organs with high $T_2$ tissue contrast. Turbo spin-echo sequences are widely used across manufacturers.

Figure 7. Body post-mortem MRI. Comparison of coronally acquired *vs* reconstructed coronal body imaging. The high-resolution isotropic constructive interference steady state sequence (b) gives much higher detail than the conventional T2-w imaging (a), particularly of the cystic dysplastic kidneys in this 21-week gestation foetus who underwent termination of pregnancy for obstructive uropathy.

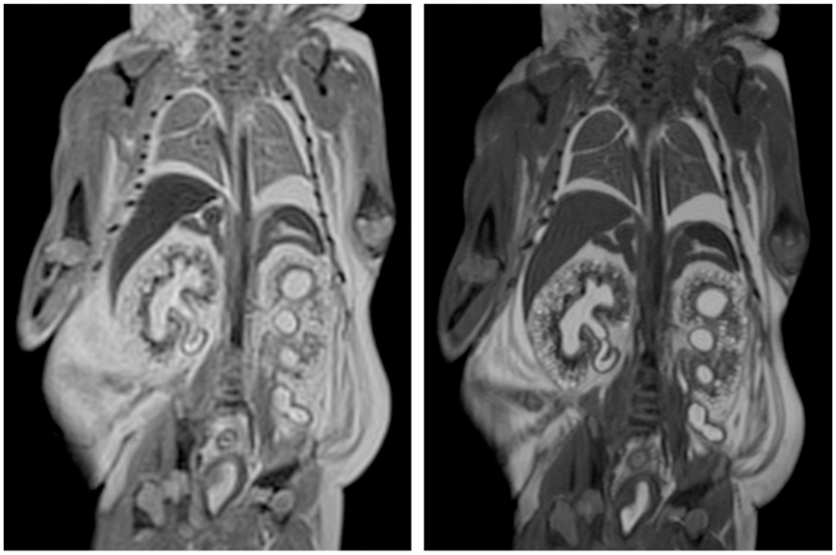

(a) (b)

Figure 8. Three-dimensional post-mortem MRI (3D PMMR) to problem-solve. 3D PMMR can be used to accurately delineate complex structures where a large abnormality which does not conform to conventional planes is suspected. Coronal reconstruction of the thorax and abdomen in a foetus with obstructive uropathy, showing a multicystic dysplastic right kidney (white arrow) and obstructed left kidney, with grossly tortuous dilated ureters (black arrow), and a thickened trabeculated bladder (not shown), representing bladder outflow obstruction. Secondary pulmonary hypoplasia is also demonstrated. Posterior urethral valves were confirmed at autopsy. Reproduced from Arthurs et al[4] with permission from Springer.

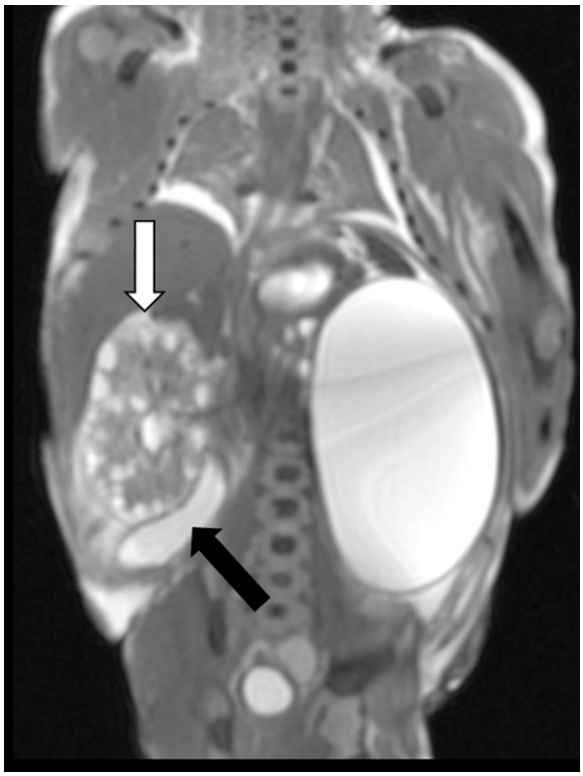

We acquire high-resolution 3D isotropic data set of the body using a 3D CISS sequence. Used in adult imaging for fine structures such as the cranial nerves or the inner auditory meatus, a 3D CISS sequence is a gradient echo sequence which gives a simulated $T_2$ echo ($T_2/T_1$ ratio).[34] Two true fast imaging with steady-state precession (TrueFISP) sequence are acquired with and without RF phase alternation and then combined for strong $T_2$ weighting into a single high resolution 3D image. When the paired data sets are combined, the phase errors cancel, effectively eliminating the normal dispersion bands which are typically seen on TrueFISP images due to patient-induced local field inhomogeneities (and emphasized by the relatively long repetition time used).

The main advantage of the 3D CISS sequence is the combination of $T_1/T_2$ contrast, high signal and very high spatial resolution, making it ideally suited to cardiac morphology assessment. The inherent flow compensation is irrelevant for post-mortem imaging. It is useful for evaluating structures that are surrounded by fluid and can detect subtle lesions that cannot be seen on routine spin echo sequences and is particularly useful for problem solving (Figures 7 and 9). With long acquisition times, it can give exquisite high-resolution imaging of all of the body organs, including the heart, lungs, liver, kidneys, bowel and vasculature. Most congenital abnormalities are detected on this sequence (Figures 6–9). The disadvantage of this sequence is that its long acquisition times with 8–10 averages can take up to 40 min to acquire.

An alternative 3D volumetric acquisition is possible with other sequences such as a SPACE (single slab 3D TSE sequence with slab selective, variable excitation pulse) sequence. This isotropic volume sequence has strong $T_2$ weighting, giving images with high signal and high spatial resolution. As image contrast is determined by the $T_2/T_1$ ratio, tissues with both long $T_2$ and short $T_1$ have high signal. The SPACE sequence is widely used in life for high resolution, contiguous, thin-section isotropic images for complex anatomy (brain, inner ear, joints). In our experience, signal to noise ratio is better with CISS, and sequence duration can

Figure 9. Three-dimensional (3D) post-mortem MRI (PMMR) to problem solve. 3D PMMR can be used to investigate internal structures in severe abnormalities. Coronal reconstruction images of the whole fetus in suspected anencephaly at 22 weeks. PMMR showed truncated thoracic spine, two kidneys and small bowel but no liver, spleen, stomach or any identifiable normal structures above the diaphragm. Autopsy was not performed to confirm these findings.

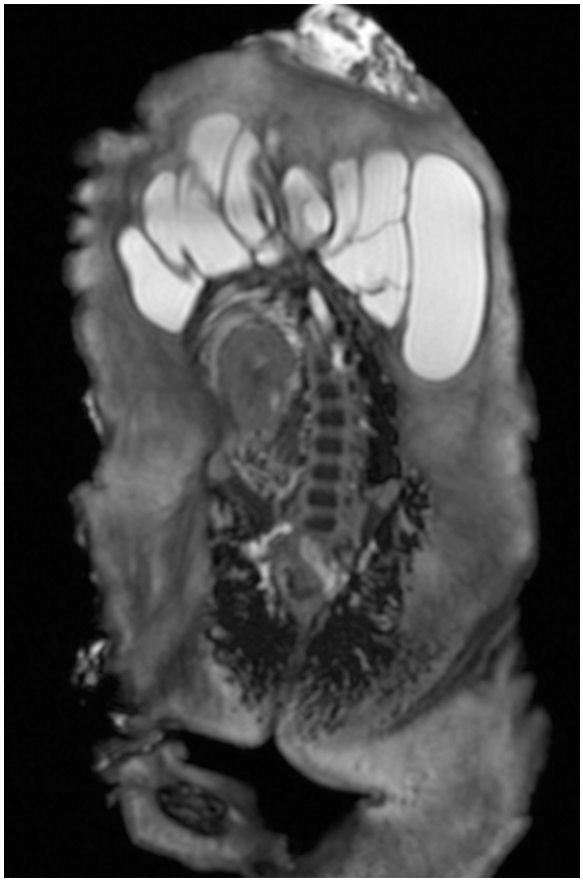

Figure 10. Limits of body post-mortem MRI (PMMR). Three-dimensional reconstruction from high-resolution constructive interference steady state image of a 13-week gestation foetus who underwent spontaneous miscarriage. High-resolution imaging at 1.5-T field strength PMMR at this gestation is limited and at low body weights is often non-diagnostic.

be shortened by using fewer averages or the addition of parallel imaging (Figures 5 and 7). Fat-suppressed steady state True-FISP imaging is available across manufacturers, including FIESTA, balanced FFE and True SSFP (GE, Phillips, Toshiba, respectively); dual excitation is known as FIESTA-C on a GE machine. The equivalent sequences to SPACE are CUBE, VISTA and 3D MVOX (GE, Phillips, Toshiba, respectively).

### Diffusion-weighted imaging

DWI of the body can also be useful and is currently an area of active research. We recently showed that liver and renal cortex ADC values were lower in PM cases than normal live infants, which may be related to different water content of different organs and their rate of autolysis or decomposition.[35] Lung ADC values were higher, likely to represent fluid accumulation in the lungs following death, since there is no signal obtained from normal aerated lung parenchyma in live infants. Interestingly, there was a significant correlation between lung ADC and post-mortem interval, which could be of interest in medicolegal cases.

### Age adaptation of protocols

Clearly, the most significant adaptation to these protocols is based on different sizes. Foetal protocols have thinner slices and smaller fields of view to allow for better resolution of small anatomical parts. However, signal to noise ratio is preserved by increasing the number of average or acquisitions for each sequence, time permitting. As electrocardiogram or respiratory gating is not typically required, increasing the number of averages far beyond that which is possible in living patients may give enhanced signal-to-noise ratios. However, one of the main limitations of foetal PMMR is foetal size which may necessitate higher field strengths (Figure 10).[36]

## CONCLUSION

We present our standardized departmental protocol for PMMR to aid those who may be considering establishing a similar service in their institution. This may also form a basis for a common protocol for future collaborative studies.

## FUNDING

AMT and OJA are supported by National Institute for Health Research (NIHR) Senior Research Fellowship and NIHR Clinician Scientist Fellowship awards, respectively. AMT receives funding from the Great Ormond Street Hospital Children's Charity and NIHR GOSH Biomedical Research Centre. This article presents independent research funded by the NIHR and supported by the Great Ormond Street Hospital Biomedical Research Centre. The views expressed are those of the author(s) and not necessarily those of the NHS, NIHR or Department of Health.

## REFERENCES

1. Ross SG, Bolliger SA, Ampanozi G, Oesterhelweg L, Thali MJ, Flach PM. Postmortem CT angiography: capabilities and limitations in traumatic and natural causes of death. *Radiographics* 2014; **34**: 830–46. doi: http://dx.doi.org/10.1148/rg.343115169
2. Grabherr S, Grimm J, Dominguez A, Vanhaebost J, Mangin P. Advances in post-mortem CT-angiography. *Br J Radiol* 2014; **87**: 20130488. doi: http://dx.doi.org/10.1259/bjr.20130488
3. Addison S, Arthurs O, Thayyil S. Post-mortem MRI as an alternative to non-forensic autopsy in foetuses and children: from research into clinical practice. *Br J Radiol* 2014; **87**: 20130621. doi: http://dx.doi.org/10.1259/bjr.20130621
4. Arthurs OJ, Taylor AM, Sebire NJ. Indications, advantages and limitations of perinatal

postmortem imaging in clinical practice. *Pediatr Radiol* 2014; **45**: 491–500. doi: http://dx.doi.org/10.1007/s00247-014-3165-z
5. Thayyil S, Sebire NJ, Chitty LS, Wade A, Chong W, Olsen O, et al. Post-mortem MRI *versus* conventional autopsy in fetuses and children: a prospective validation study. *Lancet* 2013; **382**: 223–33. doi: http://dx.doi.org/10.1016/S0140-6736(13)60134-8
6. Arthurs OJ, Barber JL, Taylor AM, Sebire NJ. Normal perinatal and paediatric postmortem magnetic resonance imaging appearances. *Pediatr Radiol* 2015; **45**: 527–35. doi: http://dx.doi.org/10.1007/s00247-014-3166-y
7. Christe A, Flach P, Ross S, Spendlove D, Bolliger S, Vock P, et al. Clinical radiology and postmortem imaging (virtopsy) are not the same: specific and unspecific postmortem signs. *Leg Med* 2010; **12**: 215–22. doi: http://dx.doi.org/10.1016/j.legalmed.2010.05.005
8. Brookes JA, Hall-Craggs MA, Sams VR, Lees WR. Non-invasive perinatal necropsy by magnetic resonance imaging. *Lancet* 1996; **348**: 1139–41. doi: http://dx.doi.org/10.1016/S0140-6736(96)02287-8
9. Woodward PJ, Sohaey R, Harris DP, Jackson GM, Klatt EC, Alexander AL, et al. Postmortem fetal MR imaging: comparison with findings at autopsy. *Obstet Gynecol Surv* 1997; **52**: 474–5. doi: http://dx.doi.org/10.2214/ajr.168.1.8976917
10. Brookes JA, Deng J, Wilkinson ID, Lees WR. Three-dimensional imaging of the postmortem fetus by MRI: early experience. *Fetal Diagn Ther* 1999; **14**: 166–71.
11. Huisman TA, Wisser J, Stallmach T, Krestin GP, Huch R, Kubik-Huch RA. MR autopsy in fetuses. *Fetal Diagn Ther* 2002; **17**: 58–64. doi: http://dx.doi.org/10.1159/000048008
12. Griffiths PD, Variend D, Evans M, Jones A, Wilkinson ID, Paley MN, et al. Postmortem MR imaging of the fetal and stillborn central nervous system. *AJNR Am J Neuroradiol* 2003; **24**: 22–7.
13. Alderliesten ME, Peringa J, Hulst VP, Blaauwgeers HL, Lith JM. Perinatal mortality: clinical value of postmortem magnetic resonance imaging compared with autopsy in routine obstetric practice. *BJOG* 2003; **110**: 378–82. doi: http://dx.doi.org/10.1046/j.1471-0528.2003.02076.x
14. Breeze A, Cross J, Hackett G, Jessop F, Joubert I, Lomas D, et al. Use of a confidence scale in reporting postmortem fetal magnetic resonance imaging. *Ultrasound Obstet Gynecol* 2006; **28**: 918–24. doi: http://dx.doi.org/10.1002/uog.3886
15. Sarikouch S, Haas NA, Schaeffler R, Beerbaum P. Value of postmortem magnetic resonance imaging for fatal neonatal congenital heart disease: a case report. *Pediatr Cardiol* 2008; **29**: 667–9. doi: http://dx.doi.org/10.1007/s00246-007-9138-3
16. Sieswerda-Hoogendoorn T, van Rijn RR. Current techniques in postmortem imaging with specific attention to paediatric applications. *Pediatr Radiol* 2010; **40**: 141–52. doi: http://dx.doi.org/10.1007/s00247-009-1486-0
17. Thayyil S, Sebire NJ, Chitty LS, Wade A, Olsen O, Gunny RS, et al. Post mortem magnetic resonance imaging in the fetus, infant and child: a comparative study with conventional autopsy (MaRIAS Protocol). *BMC Pediatr* 2011; **11**: 120. doi: http://dx.doi.org/10.1186/1471-2431-11-120
18. Prodhomme O, Seguret F, Martrille L, Pidoux O, Cambonie G, Couture A, et al. Organ volume measurements: comparison between MRI and autopsy findings in infants following sudden unexpected death. *Arch Dis Child Fetal Neonatal Ed* 2012; **97**: F434–8. doi: http://dx.doi.org/10.1136/fetalneonatal-2011-301309
19. Cannie M, Votino C, Moerman P, Vanheste R, Segers V, Van Berkel K, et al. Acceptance, reliability and confidence of diagnosis of fetal and neonatal virtuopsy compared with conventional autopsy: a prospective study. *Ultrasound Obstet Gynecol* 2012; **39**: 659–65. doi: http://dx.doi.org/10.1002/uog.10079
20. Sandaite I, De Catte L, Moerman P, Gewillig M, Fedele L, Deprest J, et al. A morphometric study of the human fetal heart on postmortem 3-tesla magnetic resonance imaging. *Prenat Diagn* 2013; **33**: 318–27. doi: http://dx.doi.org/10.1002/pd.4070
21. Arthurs O, Taylor A, Sebire N. The less-invasive perinatal autopsy: current status and future directions. *Fetal Matern Med Rev* 2013; **24**: 45–59. doi: http://dx.doi.org/10.1017/S0965539513000065
22. Kasprian G, Brugger PC, Weber M, Krssák M, Krampl E, Herold C, et al. *In utero* tractography of fetal white matter development. *Neuroimage* 2008; **43**: 213–24. doi: http://dx.doi.org/10.1016/j.neuroimage.2008.07.026
23. Garel C. The role of MRI in the evaluation of the fetal brain with an emphasis on biometry, gyration and parenchyma. *Pediatr Radiol* 2004; **34**: 694–9. doi: http://dx.doi.org/10.1007/s00247-004-1249-x
24. Glenn O, Barkovich A. Magnetic resonance imaging of the fetal brain and spine: an increasingly important tool in prenatal diagnosis, part 1. *AJNR Am J Neuroradiol* 2006; **27**: 1604–11.
25. Papadopoulou I, Sebire N, Shelmerdine S, Bower S, Arthurs O. Post mortem image-guided biopsy for less-invasive diagnosis of congenital intracranial teratoma. *Ultrasound Obstet Gynecol* 2015; **46**: 741–3. doi: http://dx.doi.org/10.1002/uog.14903
26. Hagmann P, Jonasson L, Maeder P, Thiran JP, Wedeen VJ, Meuli R. Understanding diffusion MR imaging techniques: from scalar diffusion-weighted imaging to diffusion tensor imaging and beyond 1. *Radiographics* 2006; **26**: S205–23. doi: http://dx.doi.org/10.1148/rg.26si065510
27. Le Bihan D. Apparent diffusion coefficient and beyond: what diffusion MR imaging can tell us about tissue structure. *Radiology* 2013; **268**: 318–22. doi: http://dx.doi.org/10.1148/radiol.13130420
28. Sartor A, Arthurs O, Alberti C, Belarbi N, Tilea B, Boizeau P, et al. Apparent diffusion coefficient measurements of the fetal brain during the third trimester of pregnancy: how reliable are they in clinical practice? *Prenatal Diagn* 2014; **34**: 357–66. doi: http://dx.doi.org/10.1002/pd.4309
29. Clark MA, Worrell MB, Pless JE. Postmortem changes in soft tissues. In: *Forensic taphonomy: the postmortem fate human remains*. Boca Raton, FL: CRC; 1997. pp. 151–64.
30. Shepherd TM, Flint JJ, Thelwall PE, Stanisz GJ, Mareci TH, Yachnis AT, et al. Postmortem interval alters the water relaxation and diffusion properties of rat nervous tissue—implications for MRI studies of human autopsy samples. *Neuroimage* 2009; **44**: 820–6. doi: http://dx.doi.org/10.1016/j.neuroimage.2008.09.054
31. Scheurer E, Lovblad KO, Kreis R, Maier S, Boesch C, Dirnhofer R, et al. Forensic application of postmortem diffusion-weighted and diffusion tensor MR imaging of the human brain in situ. *AJNR Am J Neuroradiol* 2011; **32**: 1518–24. doi: http://dx.doi.org/10.3174/ajnr.A2508
32. Arthurs O, Thayyil S, Wade A, Chong W, Sebire NJ, Taylor A. Normal ascent of the conus medullaris: a post-mortem foetal MRI study. *J Matern Fetal Neonatal Med* 2013; **26**: 697–702. doi: http://dx.doi.org/10.3109/14767058.2012.746307
33. Jawad N, Sebire NJ, Taylor AM, Arthurs OJ. Mechanisms of intradural gas on post mortem magnetic resonance imaging. *J Forensic Radiol Imaging* 2014; **2**: 138–42. doi: http://dx.doi.org/10.1016/j.jofri.2014.05.003
34. Casselman JW, Kuhweide R, Deimling M, Ampe W, Dehaene I, Meeus L. Constructive interference in steady state-3DFT MR imaging of the inner ear and cerebellopontine angle. *AJNR Am J Neuroradiol* 1993; **14**: 47–57.
35. Arthurs OJ, Price GC, Carmichael DW, Jones R, Norman W, Taylor AM, et al. Diffusion-weighted perinatal postmortem magnetic resonance imaging as a marker of postmortem interval. *Eur Radiol* 2015; **25**: 1399–406. doi: http://dx.doi.org/10.1007/s00330-014-3525-y
36. Jawad N, Sebire NJ, Wade A, Taylor AM, Chitty LS, Arthurs OJ. Bodyweight limits of fetal post mortem MRI at 1.5 T. *Ultrasound Obstetrics Gynecol* 2015. Epub ahead of print. doi: http://dx.doi.org/10.1002/uog.14948